Journal of The Electrochemical Society, **153** (4) C207-C212 (2006)
0013-4651/2006/153(4)/C207/6/$20.00 © The Electrochemical Society

In Situ Stress Measurements during Aluminum Deposition from $AlCl_3$-EtMeImCl Ionic Liquid

G. R. Stafford,[a,*,z] O. E. Kongstein,[a,] and G. M. Haarberg[b,*]**

[a]*National Institute of Standards and Technology, Materials Science and Engineering Laboratory, Gaithersburg, Maryland 20879, USA*
[b]*Department of Materials Technology, Norwegian University of Science and Technology, NO-7491 Trondheim, Norway*

In situ stress measurements were made during aluminum electrodeposition from Lewis acidic aluminum chloride-1-ethyl-3-methylimidazolium chloride ($AlCl_3$-EtMeImCl) using the wafer curvature method. The underpotential deposition of Al on (111)-textured Cu shows a stress response that is consistent with a two-step process where the first step involves the desorption of $AlCl_4^-$ from the Cu surface. This results in a tensile surface stress which is consistent with adsorbate-induced stress models that appear in the literature. The tensile stress is eliminated when the full incommensurate monolayer of aluminum is formed. On (111)-textured Au, the full Al monolayer results in a tensile stress that can be attributed to both lattice misfit and Al–Au alloying. The bulk deposition of Al on (111)-textured Au appears to be governed by Stranski–Krastanov three-dimensional growth. Initially a compressive stress is observed that we attribute to capillarity effects. This is followed by a rapid increase in tensile stress that is consistent with nuclei coalescence and grain boundary formation. In this region of nucleation and growth, the total stress is the superposition of both stress mechanisms and each is dependent on the deposition potential.
 [DOI: 10.1149/1.2168048]

Manuscript submitted June 28, 2005; revised manuscript received November 14, 2005. Available electronically February 21, 2006.

Electrodeposited films tend to develop sizable mechanical stresses as a result of the nucleation and growth process or from the use of solution additives and alloying elements needed to achieve desired deposition rates and mechanical properties. Often these stresses can approach or exceed the yield stress of the bulk material and can lead to loss of adhesion and the generation of bulk and surface defects. The stress observed at room temperature on a coated surface is typically the result of two different phenomena. The first, thermal stress, is present when the film is deposited at a temperature different from the service temperature and the film and substrate have different thermal expansion coefficients. The second, intrinsic stress, is caused by the manner in which the film grows and can arise from lattice-mismatched epitaxial growth, nuclei coalescence and grain growth during deposition, incorporation of impurities or side-reaction products, and phase transformations accompanied by volume changes. Although similar growth morphologies and stress development are inherent to both electrodeposited films[1] and those grown from the gas phase,[2-6] the electrodeposition community has only recently made efforts to better understand the microstructural contributions to film stress.

The direct electrodeposition of aluminum–transition metal alloys from ambient-temperature ionic liquids has recently received considerable attention. These electrolytes are prepared by combining $AlCl_3$ with certain unsymmetrical quaternary ammonium chloride salts such as 1-ethyl-3-methylimidazolium chloride (EtMeImCl). Progress in this area has recently been reviewed.[7] Among the alloys that have been successfully electrodeposited are Al–Cr,[8,9] Al–Mn,[10,11] Al–Ti,[12-15] and Al–V.[16] Many of these alloys may be of technological importance, particularly in thin-film form, because they show improved resistance to chloride-induced pitting corrosion relative to Al. Although these alloy films may exhibit several of the electrochemical properties required of functional coatings, the stresses associated with their formation are virtually unknown. The purpose of this paper is to examine the stresses associated with the earliest stages of aluminum deposition from the ambient temperature aluminum chloride-1-ethyl-3-methylimidazolium chloride ($AlCl_3$-EtMeImCl) ionic liquid. The in-plane stress generated in the aluminum deposit during growth was calculated from the perpendicular deflection of a flexible cathode. The deflection was measured by a laser beam reflected off of the back surface.[17-21] This and similar in situ techniques have been widely used to examine adsorbate-induced surface stress,[21-28] underpotential deposition,[29-33] electrochemical insertion and intercalation reactions,[17,18,20,34] and bulk film deposition.[35-38]

Experimental

A schematic of the components of the in situ stress measurement apparatus is shown in Fig. 1. The light source was a 1-mW helium–neon laser (JDS[c] Uniphase, model 1108P). A beam splitter (50% reflected, 50% transmitted) was placed in the path of the beam to direct the laser to the back of the cantilever working electrode, yet allow the beam reflected from the cantilever to reach the position sensing detector (PSD). The incident and reflected beams were initially coincident. Two mirrors were placed in the path of the reflected laser beam in order to increase the optical lever. A duo-lateral PSD with dimensions 20×20 mm (DLS-20 from UTD Sensors, Inc.) was used to measure the position of the reflected beam. The four photocurrents from the PSD were amplified, measured by a National Instruments A/D card, and transferred to a Macintosh Power PC computer. The signals were converted into vertical and horizontal positions on the PSD. The stress calculation utilized only the vertical position of the laser.

The cantilever was a borosilicate glass slide (D 263, Schott) measuring $60 \times 3 \times 0.108$ mm. The glass had a Young's modulus of 72.9×10^9 N m^{-2} and a Poisson ratio of 0.208, as specified by the vendor. To one side of this substrate a 4-nm-thick adhesion layer of titanium and a 250-nm film of gold were vapor-deposited by electron-beam evaporation. The glass–metal interface provided the reflective surface for the laser beam. Prior to use, the electrodes were boiled in distilled water and then held in a hydrogen flame for approximately 1 s. The Au electrodes had a strong (111) crystallographic orientation. The 200 reflection was not apparent in θ-2θ X-ray scans, and rocking curves of the 111 reflection generally yielded a full width at half-maximum on the order of 2°. The deposition of Al was examined on both (111)-textured Au and Cu electrodes. The Cu electrodes were formed by electrodepositing 0.25 μm of Cu from an additive-free copper sulfate electrolyte (0.01 mol L^{-1} $CuSO_4$ in 0.1 mol L^{-1} H_2SO_4) onto the evaporated

* Electrochemical Society Active Member.
** Electrochemical Society Student Member.
z E-mail: gery.stafford@nist.gov

[c]Certain trade names are mentioned for experimental information only; in no case does it imply a recommendation or endorsement by the National Institute of Standards and Technology.

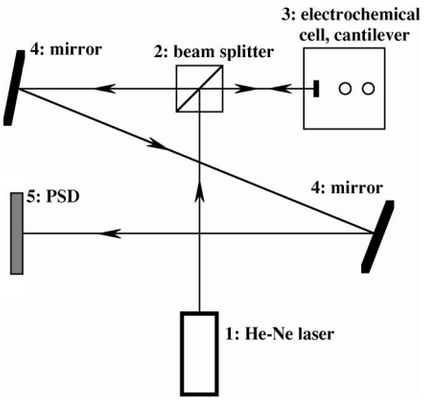

Figure 1. The laser path: (1) He–Ne laser, (2) beam splitter, (3) electrochemical cell, (4) mirrors, and (5) PSD.

Au electrodes. Examination by X-ray diffraction indicated that the Cu deposit had retained the (111) crystallographic orientation of the Au substrate.

The electrochemical cell was a single-compartment Pyrex cell. A schematic is shown in Fig. 2. A glass disk was joined to the back of the cell to allow the cell to be held and positioned by a standard mirror mount on the optical bench. The three electrodes were held in place by a segmented aluminum disk. Each of the three segments of the disk acted as a current collector for one of the electrodes; consequently, they were electrically isolated from each other. After positioning the electrodes, the disk segments were held together by plastic screws. When the disk was placed into the collar of the electrochemical cell, each segment of the disk rested on a Au-plated tungsten wire, which passed through the wall of the glass cell. The entire electrochemical cell was then sealed by a Teflon screw cap onto a compression O-ring. The cap was long enough to contact the segmented aluminum disk so that slight pressure was maintained between the disk segments and the tungsten wire feed-throughs in order to maintain electrical continuity.

The electrolyte was a 55–45 mole ratio of $AlCl_3$-EtMeImCl. It was prepared and purified using the procedures outlined in Ref. 39. The counter electrode was an aluminum wire placed parallel to and in the same solution as the working electrode. The reference electrode was also an aluminum wire placed in the same solution as the working electrode and positioned as shown in Fig. 2. All potentials reported here are with respect to the Al reference. The electrolyte was added to the cell while in a dry box containing less than 2 ppm oxygen and was then sealed. The cell was then removed from the dry box, placed in the optical mount, and positioned on the optical bench. Potential control was maintained using an EG&G Princeton

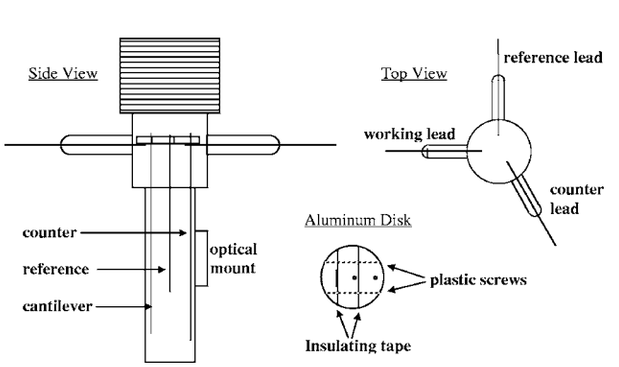

Figure 2. Schematic of electrochemical cell and aluminum disk electrode holder.

Applied Research Corp. (PARC) model 273 potentiostat/galvanostat that was controlled by a Macintosh Power PC computer and LabView software.

We examined both the changes in surface stress of the Au cantilever in response to changes in surface chemistry in the double layer and aluminum underpotential deposition (UPD) region as well as the in-plane stress developed in electrodeposited aluminum films. Because the Au electrode is on the side away from the laser, compressive stress displaces the cantilever toward the laser while tensile stress displaces the cantilever away from the laser. The relationship between the force per cantilever beam width, F_w, exerted by processes occurring on the electrode surface and the radius of curvature of the cantilever, is given by Stoney's equation[40]

$$F_w = \frac{E_s t_s^2}{6(1-\nu_s)R} = \sigma_f^{\text{avg}} t_f \qquad [1]$$

where E_s, υ_s, and t_s are the Young's modulus, Poisson ratio, and thickness of the glass substrate, respectively, and R is the radius of curvature of the cantilever. In the case where the force on the cantilever is due to surface processes, F_w is the surface stress, i.e., the reversible work per unit area needed to elastically stretch a preexisting surface, and has units of J/m^2 or N/m. For solid electrodes in solution, the surface stress is determined by the charge density at the surface, which in turn is strongly influenced by the electrode potential and adsorbates on the electrode surface. In the case where the force on the cantilever is the result of bulk metal deposition, then F_w is equal to the average biaxial stress in the electrodeposit (σ_f^{avg}) multiplied by the average deposit thickness (t_f). The film thickness was calculated from the charge, assuming 100% current efficiency and uniform current distribution. This simplified version of Stoney's equation requires only the elastic properties of the substrate. The properties of the Au film and the electrodeposit can be ignored if the combined thickness is less than 5% of the substrate thickness.[41] We have thus limited our experiments to deposit thicknesses less than 1 μm. Equation 2 is Stoney's equation in terms of the PSD output

$$F_w = \frac{E_s \cdot t_s^2 n_{\text{air}}\, d_{\text{PSD}}}{6(1-\nu_s)2Ln_{\text{el}}D_{\text{PSD}}} \qquad [2]$$

where d_{PSD} is the vertical coordinate of the reflected laser beam onto the PSD, D_{PSD} is the distance of the PSD from the electrode, and L is the length of electrode submerged into the electrolyte down to where the laser strikes the electrode. Because the electrochemical cell is filled with electrolyte, a correction must be made to account for the difference in the refractive index between the electrolyte inside the cell ($n_{\text{el}} = 1.5$) and the air outside the cell ($n_{\text{air}} = 1.0$). During a measurement F_w is determined from d_{PSD} using Eq. 2. In the configuration used for these experiments, this apparatus can resolve surface stresses on the order of 0.025 N/m. A more detailed description of the optical bench and stress measurement can be found in Ref. 42.

Results and Discussion

It has previously been reported that the UPD of Al onto Cu(111) is characterized by two pairs of well-resolved peaks, indicating the formation and dissolution of two different adsorbed structures.[43] High-resolution scanning tunneling microscopy imaging at 0.455 V revealed an ordered adlayer which was interpreted to be a layer of $AlCl_4^-$ that had been oxidatively adsorbed on the Cu(111) surface with the face of the tetrahedra adjacent to the copper surface. It was concluded that the first UPD wave involved the desorption of $AlCl_4^-$ from the Cu(111) surface. The second cathodic peak was associated with a fully discharged monolayer of aluminum on the Cu surface.

Figure 3 shows the linear sweep voltammetry and the surface stress (F_w) for the UPD of Al onto (111)-textured Cu. Although the quality of the voltammetry with respect to peak resolution is inferior to that reported on single-crystal Cu(111),[43] it is clear that the UPD process involves two distinct electrochemical steps. The surface stress curve in Fig. 3 is similar to that reported for Cu UPD on

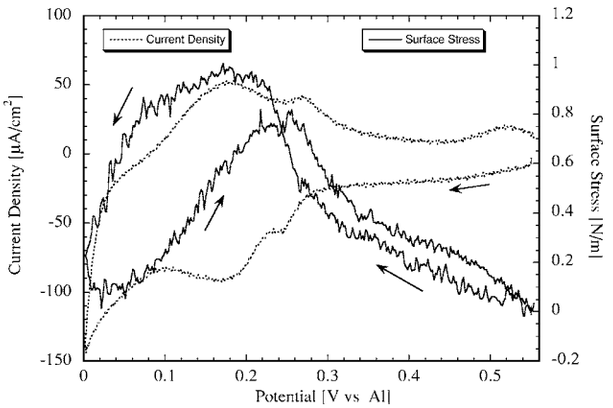

Figure 3. Linear sweep voltammetry and surface stress associated with the UPD of Al onto (111)-textured Cu in 55–45 mole ratio of $AlCl_3$-EtMeImCl. Sweep rate was 20 mV/s.

Au(111) in aqueous sulfate electrolyte,[29,31] where the change in surface stress in the tensile (positive) direction as the potential was swept cathodically was attributed to the desorption of sulfate from the electrode surface. A simple surface-induced charge redistribution model has been used to explain the stress behavior in both the sulfate adsorption and the Cu UPD regions. Ibach[23,26] has suggested that the loss of bonds at a clean metal surface causes an increased charge density between the remaining surface atoms, thereby increasing their attractive interaction and resulting in a tensile stress at the surface. This tensile stress, which has been estimated to be 2.7 N m^{-1} for Au(111),[44] has been observed in most free-electron metals and is a likely driving force for surface reconstruction.[28] As negative charge is removed from the electrode with an increase in potential the surface stress moves in the negative (compressive) direction. Likewise, when negative charge is added to the electrode with a decrease in potential the surface stress moves in the positive (tensile) direction.

The adsorption of species on the surface can also be expected to alter the surface stress because the local interaction of each adsorbate will alter the bond strength between neighboring atoms on the surface. Electron donors would be expected to cause tensile stress because they increase the bond charge density between the underlying metal atoms. Electron acceptors such as adsorbed anions cause compressive stress because they reduce the electron density in the metal surface. For example, the adsorption of a sulfate ion increases the compressive trend in the surface stress while its desorption moves the surface stress in the tensile direction. In the present case, anion adsorption (presumably $AlCl_4^-$) at more positive potentials causes a compressive shift in the surface stress of the Cu electrode. As the potential is swept cathodically and $AlCl_4^-$ is desorbed from the Cu surface, the stress moves in the tensile direction, which is consistent with the charge-induced surface stress model described above.

The formation of the complete Al monolayer results in a compressive change in the surface stress. Because the aluminum atom is 12% larger than copper, the Al monolayer is expected to be incommensurate with respect to the copper surface. As a consequence, misfit stress is not expected to play a role in the stress development. Al is likely to have a more negative potential of zero charge than Cu; thus, $AlCl_4^-$ may readsorb onto the electrode surface once the aluminum monolayer has formed. This would move the surface stress in a negative (compressive) direction. In summary, we conclude that the stress response at positive potentials reflects the adsorption/desorption of $AlCl_4^-$ from the Cu surface. The compressive stress associated with Al monolayer formation is likely due to the combination of monolayer formation and readsorption of $AlCl_4^-$ onto the newly formed Al surface.

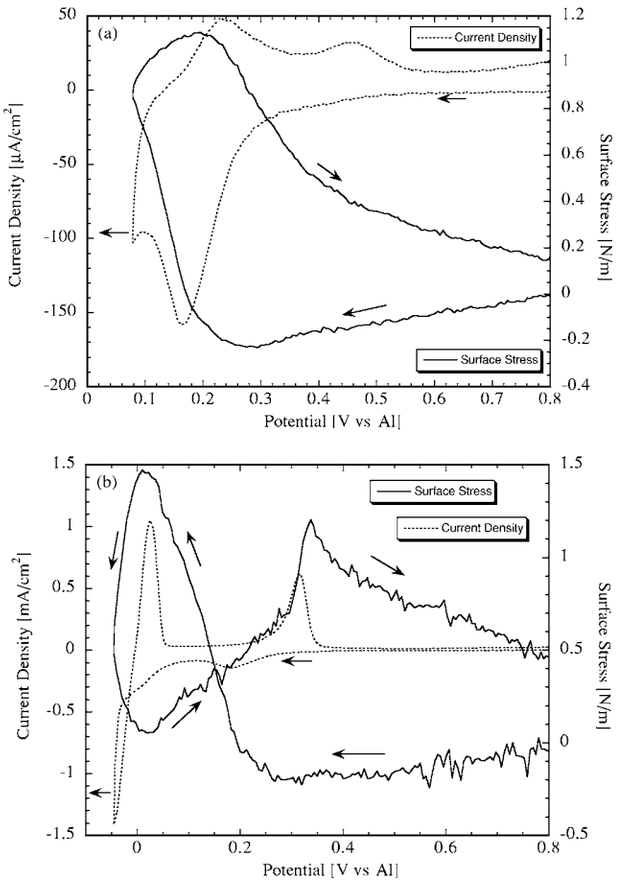

Figure 4. (a) Linear sweep voltammetry and surface stress associated with the UPD of Al onto (111)-textured Au in 55–45 mole ratio of $AlCl_3$-EtMeImCl, (b) extended down to potential for bulk Al deposition. Sweep rate was 20 mV/s.

Figure 4a shows the linear sweep voltammetry as well as the surface stress for the UPD of Al onto (111)-textured Au. The voltammetry shows a single cathodic peak at 0.165 V and two anodic peaks at 0.24 and 0.45 V. Reports in the literature indicate that Al–Au alloys can be formed in the UPD region.[45-47] The general consensus in the literature is that the first anodic peak is associated with dealloying rather than partial removal of the UPD layer. This conclusion is based on the fact that the height of the first oxidation wave increases with the time at which the electrode is held at +0.10 V. Integration of the single cathodic peak in Fig. 4a results in a charge of about 0.72 mC/cm^2, which is consistent with the theoretical value of 0.66 mC/cm^2 for a complete monolayer of Al on Au. This suggests that alloying can be minimized if the potential is simply swept through the UPD region and not held for a time to allow alloying to occur.

When the potential of the Au electrode is decreased from 0.8 to 0.3 V, the surface stress (F_w) decreases slightly in the compressive direction. This is somewhat surprising because the charge distribution model for surface stress predicts a tensile stress as electrons are added to the electrode. Further, any anion desorption process that might occur is also expected to produce a tensile stress. A possible explanation for the decrease in surface stress in this potential region is that the Au(111) surface is undergoing surface reconstruction. As the potential is reduced further, a tensile stress of about 1.2 N/m is associated with the cathodic UPD process at 0.165 V. The stress continues to increase until the first anodic wave occurs, after which the stress returns to a value somewhat higher than its original value.

One possible source of this tensile stress in the Al UPD region is the small misfit between the Al and Au lattice; the Al lattice is only 0.74% smaller than that of Au. If the Al atoms occupy the three-fold sites of the Au surface, then the Al monolayer will be under a slight tensile stress. One can estimate this stress, assuming that continuum elasticity properly describes the Al monolayer. The surface stress caused by the misfit is described in Ref. 26 by

$$\tau = \frac{Y_{(111)}}{1 - \upsilon_{(111)}} \varepsilon_{mf} d_{(111)} \theta \qquad [3]$$

where $Y_{(111)}$ is Young's modulus for single-crystal Al, $\upsilon_{(111)}$ is the Poisson ratio, ε_{mf} is the misfit strain, $d_{(111)}$ is the height of the monolayer, and θ is the number of monolayers on the surface. The elastic constants, calculated from the elastic compliances for Al,[48] are $Y_{(111)} = 72$ GPa and $\upsilon_{(111)} = 0.365$. Inserting these values into Eq. 3 for a monolayer of aluminum results in a misfit stress of +0.24 N/m, which is about 20% of that measured experimentally.

The fact that the cantilever position does not immediately return to its original value suggests that some alloying occurs between Al and Au. However, the cantilever will return to its original position if left for several minutes at a potential of 0.8 V. The formation of Al–Au alloys has been examined in some detail at higher temperatures in $AlCl_3$–NaCl electrolyte.[45] The presence of both $AlAu_2$ and Al_2Au_5 has been confirmed after 2 h at 250°C. An Arrhenius plot of the high-temperature data suggests that at 25°C an Al–Au diffusion zone of 0.27 nm will form after 60 s. The stress associated with alloy formation can be estimated from the molar volumes of the constituents and reaction product

$$\sigma_{imc} = -E'_{imc} \frac{\Delta V}{3V} \qquad [4]$$

where E'_{imc} is the biaxial modulus of the intermetallic and ΔV is the change in volume when the intermetallic forms. The molar volumes for Al and Au are 9.99 and 10.2 cm^3/mol, respectively, whereas the molar volume for orthorhombic $AlAu_2$ is 9.553 cm^3/mol. If one assumes an E'_{imc} of 200 GPa and includes the $\Delta V/V$ of −0.056, then alloying will produce a force on the cantilever of +3.7 N/m for each nanometer of intermetallic formed. The 0.27 nm of $AlAu_2$ formed in 60 s, estimated from the high-temperature kinetic data, would result in a surface stress of +1.0 N/m, which is close to that observed experimentally. It is clear that both surface alloying and lattice misfit can account for the tensile stress observed during Al UPD on Au.

Figure 4b shows that when the potential is decreased to the point of bulk Al deposition, the stress moves in the compressive direction. When the bulk Al is electrochemically stripped, the stress moves in the tensile direction, reflecting the condition established by the first monolayer. The changes in stress during dissolution are far more sluggish than those during deposition. This may be another indication that alloying is taking place. When the potential reaches 800 mV, there is a net tensile stress of about 0.5 N/m, again reflecting the alloying between Al and Au. With time at elevated potential, the stress returns to its original starting value of zero, suggesting that the surface alloy does not permanently alter the Au cantilever electrode.

The intrinsic stress associated with the bulk deposition of aluminum was examined by pulsing the potential of the cantilever electrode to a series of cathodic values. Figure 5 shows the chronoamperograms associated with those potential pulses. The transients show the current increase and Cottrell relaxation that is typical of three-dimensional nucleation as the spherical diffusion fields overlap into a single linear diffusion front. One can conclude that aluminum deposition occurs by three-dimensional nucleation followed by diffusion-controlled growth. This suggests that the growth follows Stranski–Krastanov growth where the initial wetting layer transforms to island growth as the deposit thickens. The nucleation chronoamperograms were also normalized to the current/time maxima in the traditional way to shed light on the nucleation kinetics.[49] The data showed a reasonable fit to the theoretical curve for instantaneous nucleation.

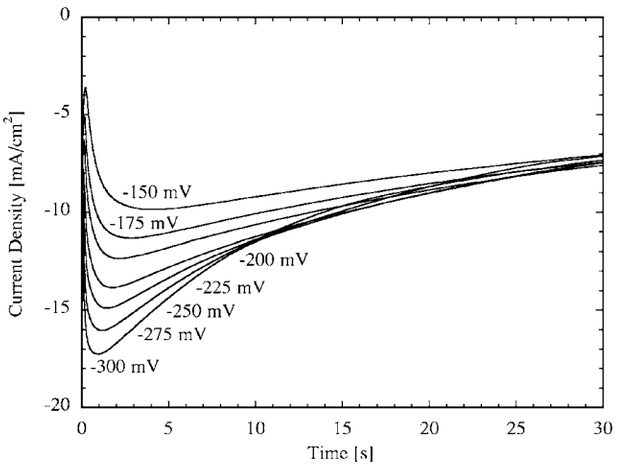

Figure 5. Chronoamperograms for Al deposition onto (111)-textured Au in 55–45 mole ratio of $AlCl_3$-EtMeImCl. The potential was stepped from +0.3 V to a deposition potential ranging from −0.05 to −0.25 V in 0.025-V increments.

Figure 6a shows the F_w associated with the bulk deposition of aluminum for a film thickness up to 260 nm. The negative F_w indicates that the Al films develop a compressive stress in the earliest stages of growth. The incremental film stress, given by the slope of the F_w—thickness curve, is also seen to increase in the negative direction with increasing deposition overpotential. At a given deposit thickness that is dependent on the electrode potential, the cantilever F_w begins to move in the tensile direction until a net tensile stress is established. Figure 6b shows the average film stress (F_w divided by the film thickness) obtained from the F_w—thickness curves in Fig. 6a. As the overpotential is increased, the compressive stresses in the early stages of deposition increase from −50 to −120 MPa. The stress then becomes tensile and both the thickness at which the transition occurs and the magnitude of the tensile excursion are a function of deposition potential. A maximum tensile stress of 70 MPa was observed in the film deposited at −300 mV.

The growth stresses associated with Volmer–Weber or island growth from the gas phase have been divided into three distinct modes:[2-6] low-mobility columnar growth, epitaxial growth, and high-mobility island growth. The low-mobility columnar films develop tensile stresses, epitaxial Volmer–Weber films are completely compressive, while high-mobility films show a tensile to compressive transition as the film thickens. The general observation in the latter case is that the stress progresses from compressive to tensile and then back to compressive. This has been referred to as CTC behavior. The initial compressive stress occurs in the discrete-nuclei stage of growth and is due to the capillarity stress of these small particles. The rapid development of tensile stress is associated with nuclei coalescence and grain boundary formation while the final compressive stage occurs during thickening of the continuous film.

The nucleation transients in Fig. 5 indicate that the aluminum films grow by three-dimensional nucleation and diffusion-controlled growth. As a consequence, one would expect to observe a compressive to tensile transition in the stress transient. As noted in the literature, the compressive stress in the earliest stages of deposition is due to the capillarity stress associated with small particles. This is similar to the pressure inside a small drop of liquid which is related to the drop radius by the Laplace equation. A similar treatment can be used to characterize the strain in a solid particle. For a spherical solid particle

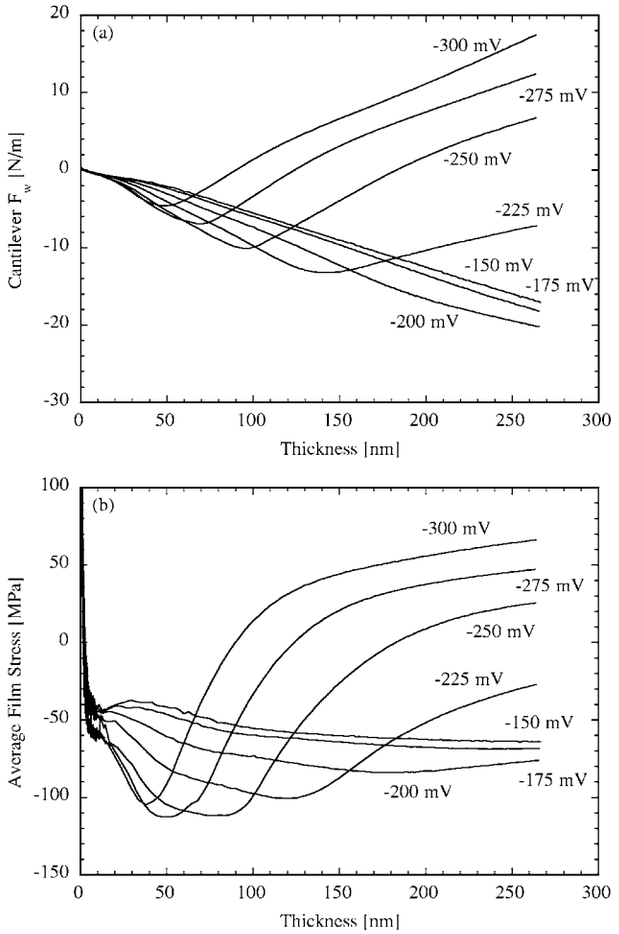

Figure 6. (a) Force per cantilever beam width, F_w, and (b) the average film stress, σ_f^{avg}, plotted as a function of deposit thickness (up to 260 nm) for Al deposited onto (111)-textured Au in 55–45 mole ratio of $AlCl_3$-EtMeImCl, as a function of deposition potential.

$$\Delta P = -\frac{2f}{r} \quad [5]$$

where f is the surface stress, r is the particle radius, and ΔP is the pressure difference. Using the definition of the bulk modulus of a solid, $K = -\Delta PV/\Delta V$ where V is the volume, and assuming that the nuclei are crystalline and have a cubic structure with lattice parameter a, the equilibrium lattice parameter as a function of the distance r from the particle center is[2]

$$a(r) = a_o\left|1 - \frac{2f}{3Kr}\right| \quad [6]$$

where K is the bulk modulus of the particle and a_o is the equilibrium lattice parameter of the bulk material. The atomic distances associated with small particles are compressed when compared to the equilibrium parameter of the bulk material. In fact, the earliest surface stress determinations were made from lattice parameter measurements of small metallic particles, typically less than 15 nm in diameter.[50-52] It is important to note that these small particles are in equilibrium and do not exert a stress on the cantilever substrate (other than a possible misfit stress). The basic mechanism for stress generation is associated with particle growth. When the particles nucleate on the surface, they have a lattice parameter that is dictated by the particle radius. As the particle grows, the equilibrium lattice parameter increases. Once the nuclei become rigidly attached to the substrate, the lattice parameter cannot adjust to the equilibrium value and the nuclei develop a positive stress-free strain. An in-plane, biaxial compressive stress (σ) is generated that is related to the strain in the particle (ε) by

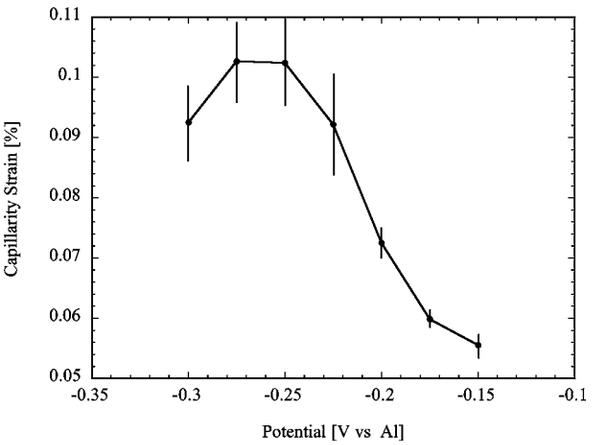

Figure 7. Nuclei strain calculated from Eq. 7 using the maximum compressive stresses taken from the stress-thickness transients (as in Fig. 6b). The data points are an average of three independent measurements. The error bars represent the standard deviation of those measurements.

$$\sigma = -E'\varepsilon \quad [7]$$

where E' is the biaxial modulus. Figure 7 is a plot of the strain that was calculated from the maximum compressive stresses taken from stress-thickness transients similar to those shown in Fig. 6b. A value of 113 GPa was used for the biaxial modulus (E') of aluminum. This should be viewed as an estimate of the strain since a uniform deposit thickness was assumed in calculating the average film stress. The strain is seen to increase with increasing deposition overpotential. The apparent decrease in strain at the highest overpotentials is most likely the result of nuclei coalescence that occurs before the full strain is established in the nuclei (see Fig. 6b). The 0.05–0.1% strains that were calculated from the compressive stresses are consistent with values that might be expected due to capillarity. A more detailed description of the film stress induced by surface stresses for the growth of cylindrical islands has been derived in the literature.[3,53]

The stress curves can also be used to estimate the nucleation density at the point of coalescence if one assumes that the minimum in the stress-thickness curve occurs when the nuclei first touch and begin to form grain boundaries.[53] In other words, the capillarity stress remains constant while tensile stress due to coalescence begins to move the average film stress in the positive direction. If it is assumed that the nuclei are hemispherical in shape, of equal size, and are distributed to form a square grid, then the nucleation density and nuclei radius can be calculated from Eq. 8 where N is the nucleation density and t is the average deposit thickness

$$N = \frac{0.068}{t^2}, \quad r = \frac{0.5}{N^{1/2}} \quad [8]$$

Figure 8 shows a plot of both the nucleation density and nuclei radius at coalescence as a function of the deposition overpotential from the nominal deposit thickness taken from the stress minima in Fig. 6b. The nucleation density varies from 10^8 to 10^{10} cm^{-2}, which is consistent with values that are typically measured microscopically on electrodeposited films.[49,54] The nucleation density is also seen to increase with deposition overpotential, which is consistent with electrocrystallization theory and experimental observation reported in the literature. Similarly, the radius of the nuclei, calculated from the nucleation densities, range in size from 60 to 500 nm. At coalescence, this would result in aluminum grains on the order of 0.1–1 μm diam, which are very realistic values.

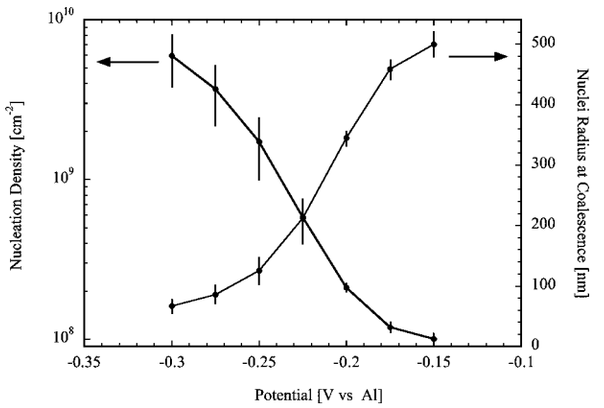

Figure 8. Plots of nucleation density and particle radius at coalescence, calculated from the thickness taken at maximum compressive stress in Fig. 6b, as a function of deposition overpotential. The data points are an average of four independent measurements. The error bars represent the standard deviation of those measurements.

Conclusion

In situ stress measurements were made during aluminum electrodeposition from $AlCl_3$-EtMeImCl using the wafer curvature method. The UPD of Al on (111)-textured Cu shows a stress response that is consistent with a two-step process where the first step involves the desorption of $AlCl_4^-$. This gives rise to a tensile shift in the surface stress. The tensile stress is eliminated when the full incommensurate monolayer of aluminum is formed. The situation is very different on (111)-textured Au. In this case a compressive shift is observed as the potential is swept cathodically in the potential region positive of aluminum UPD. This is inconsistent with charge distribution models that appear in the literature. The full Al monolayer results in a tensile stress that can be attributed to both lattice misfit and Al–Au alloying. The bulk deposition of Al on (111)-textured Au appears to be governed by Stranski–Krastanov three-dimensional growth. Initially a compressive stress is observed that we attribute to capillarity. This is followed by a rapid increase in tensile stress that we attribute to nuclei coalescence and grain boundary formation. In this region of film formation, the total stress is the superposition of both stress mechanisms and each shows a dependence on the deposition potential.

Acknowledgments

The authors gratefully acknowledge the technical contributions of Thomas Moffat, Jonathon Guyer, Charles Hussey, and Vladimir Jovic.

National Institute of Standards and Technology assisted in meeting the publication costs of this article.

References

1. R. Weil, *Plating*, **58**, 50 (1971).
2. R. Koch, *J. Phys.: Condens. Matter*, **6**, 9519 (1994).
3. J. A. Floro, E. Chason, R. C. Cammarata, and D. J. Srolovitz, *MRS Bull.*, **27**, 19 (2002).
4. A. L. Shull and F. Spaepen, *J. Appl. Phys.*, **80**, 6243 (1996).
5. W. D. Nix and B. M. Clemens, *J. Mater. Res.*, **14**, 3467 (1999).
6. R. Abermann, *Vacuum*, **41**, 1279 (1990).
7. G. R. Stafford and C. L. Hussey, in *Advances in Electrochemical Science and Engineering*, Vol., 7, R. C. Alkire and D. M. Kolb, Editors, p. 275, Wiley-VCH Verlag GmbH, Weinheim, Germany (2002).
8. T. P. Moffat, *J. Electrochem. Soc.*, **141**, L115 (1994).
9. M. R. Ali, A. Nishikata, and T. Tsuru, *Electrochim. Acta*, **42**, 2347 (1997).
10. G. R. Stafford, *J. Electrochem. Soc.*, **136**, 635 (1989).
11. T. P. Moffat, G. R. Stafford, and D. E. Hall, *J. Electrochem. Soc.*, **140**, 2779 (1993).
12. G. M. Janowski and G. R. Stafford, *Metall. Trans. A*, **23A**, 2715 (1992).
13. G. R. Stafford, *J. Electrochem. Soc.*, **141**, 245 (1994).
14. T. Takenaka, A. Hoshikawa, and M. Kawakami, in *International Symposium on Molten Salt Chemistry and Technology-1993*, PV 93-9, p. 184, M.-L. Saboungi and H. Kojima, Editors, The Electrochemical Society Proceedings Series, Pennington, New Jersey (1993).
15. T. Tsuda, C. L. Hussey, G. R. Stafford, and J. E. Bonevich, *J. Electrochem. Soc.*, **150**, C234 (2003).
16. G. R. Stafford, T. Tsuda, and C. L. Hussey, *J. Min. Metall., B*, **39**, 23 (2003).
17. J. Scarminio, S. N. Sahu, and F. Decker, *J. Phys. E*, **22**, 755 (1989).
18. J. M. Rosolen and F. Decker, *J. Electrochem. Soc.*, **143**, 2417 (1996).
19. G. G. Lang and M. Seo, *J. Electroanal. Chem.*, **490**, 98 (2000).
20. K. Y. Chung and K.-B. Kim, *J. Electrochem. Soc.*, **149**, A79 (2002).
21. M. Seo and Y. Serizawa, *J. Electrochem. Soc.*, **150**, E472 (2003).
22. L. Jaeckel, G. Lang, and K. E. Heusler, *Electrochim. Acta*, **39**, 1031 (1994).
23. H. Ibach, *J. Vac. Sci. Technol. A*, **A12**, 2240 (1994).
24. R. Raiteri and H.-J. Butt, *J. Phys. Chem.*, **99**, 15728 (1995).
25. T. A. Brunt, E. D. Chabala, T. Rayment, S. J. O'Shea, and M. E. Welland, *J. Chem. Soc., Faraday Trans.*, **92**, 3807 (1996).
26. H. Ibach, *Surf. Sci. Rep.*, **29**, 193 (1997).
27. W. Haiss, R. J. Nichols, J. K. Sass, and K. P. Charle, *J. Electroanal. Chem.*, **452**, 199 (1998).
28. W. Haiss, *Rep. Prog. Phys.*, **64**, 591 (2001).
29. W. Haiss and J. K. Sass, *J. Electroanal. Chem.*, **386**, 267 (1995).
30. T. A. Brunt, T. Rayment, S. J. O'Shea, and M. E. Welland, *Langmuir*, **12**, 5942 (1996).
31. W. Haiss and J. K. Sass, *Langmuir*, **12**, 4311 (1996).
32. W. Haiss and J. K. Sass, *J. Electroanal. Chem.*, **410**, 119 (1996).
33. C. Friesen, N. Dimitrov, R. C. Cammarata, and K. Sieradzki, *Langmuir*, **17**, 807 (2001).
34. S. N. Sahu, J. Scarminio, and F. Decker, *J. Electrochem. Soc.*, **137**, 1150 (1990).
35. R. Weil, *Plating*, **58**, 137 (1971).
36. M. A. Butler and D. S. Ginley, *J. Electrochem. Soc.*, **134**, 510 (1987).
37. H. Feigenbaum and R. Weil, *J. Electrochem. Soc.*, **126**, 2085 (1979).
38. W. Haiss, R. J. Nichols, and J. K. Sass, *Surf. Sci.*, **388**, 141 (1997).
39. J. S. Wilkes, J. A. Levisky, R. A. Wilson, and C. L. Hussey, *Inorg. Chem.*, **21**, 1263 (1982).
40. G. G. Stoney, *Proc. R. Soc. London, Ser. A*, **82**, 172 (1909).
41. G. Moulard, G. Contoux, G. Motyl, G. Gardet, and M. Courbon, *J. Vac. Sci. Technol. A*, **16**, 736 (1998).
42. O. E. Kongstein, U. Bertocci, and G. R. Stafford, *J. Electrochem. Soc.*, **152**, C116 (2005).
43. G. R. Stafford, V. D. Jovic, T. P. Moffat, Q. Zhu, S. Jones, and C. L. Hussey, in *Twelfth International Symposium on Molten Salts*, PV 99-41, p. 535, P. C. Trulove, H. C. De Long, G. R. Stafford, and S. Deki, Editors, The Electrochemical Society Proceedings Series, Pennington, New Jersey (1999).
44. V. Fiorentini, M. Methfessel, and M. Scheffler, *Phys. Rev. Lett.*, **71**, 1051 (1993).
45. B. S. Radovic, R. A. H. Edwards, and J. N. Jovicevic, *J. Electroanal. Chem.*, **428**, 113 (1997).
46. C. A. Zell, F. Endres, and W. Freyland, *Phys. Chem. Chem. Phys.*, **1**, 697 (1999).
47. J.-J. Lee, I. T. Bae, D. A. Scherson, B. Miller, and K. A. Wheeler, *J. Electrochem. Soc.*, **147**, 562 (2000).
48. G. Simmons and H. Wang, *Single Crystal Elastic Constants and Calculated Aggregate Properties: A Handbook*, The M.I.T. Press, Cambridge, MA, (1971).
49. B. Scharifker and G. Hills, *Electrochim. Acta*, **28**, 879 (1983).
50. C. W. Mays, J. S. Vermaak, and D. Kuhlmann-Wilsdorf, *Surf. Sci.*, **12**, 134 (1968).
51. H. J. Wasserman and J. S. Vermaak, *Surf. Sci.*, **22**, 164 (1970).
52. H. J. Wasserman and J. S. Vermaak, *Surf. Sci.*, **32**, 168 (1972).
53. R. C. Cammarata, T. M. Trimble, and D. J. Srolovitz, *J. Mater. Res.*, **15**, 2468 (2000).
54. A. Radisic, A. C. West, and P. C. Searson, *J. Electrochem. Soc.*, **149**, C94 (2002).